



HAL
open science

Impact of Fluidized Granular Flows into Water: Implications for Tsunamis Generated by Pyroclastic Flows

Alexis Bougouin, Raphael Paris, Olivier Roche

► **To cite this version:**

Alexis Bougouin, Raphael Paris, Olivier Roche. Impact of Fluidized Granular Flows into Water: Implications for Tsunamis Generated by Pyroclastic Flows. *Journal of Geophysical Research : Solid Earth*, 2020, 125 (5), 10.1029/2019JB018954 . hal-02794348

HAL Id: hal-02794348

<https://uca.hal.science/hal-02794348>

Submitted on 4 Sep 2020

HAL is a multi-disciplinary open access archive for the deposit and dissemination of scientific research documents, whether they are published or not. The documents may come from teaching and research institutions in France or abroad, or from public or private research centers.

L'archive ouverte pluridisciplinaire **HAL**, est destinée au dépôt et à la diffusion de documents scientifiques de niveau recherche, publiés ou non, émanant des établissements d'enseignement et de recherche français ou étrangers, des laboratoires publics ou privés.

1 **Impact of fluidized granular flows into water:**
2 **Implications for tsunamis generated by pyroclastic**
3 **flows**

4 **A. Bougouin, R. Paris, and O. Roche**

5 Université Clermont Auvergne, CNRS, IRD, OPGC, Laboratoire Magmas et Volcans, F-63000
6 Clermont-Ferrand, France

7 **Key Points:**

- 8 • Novel laboratory experiments of fluidized granular flows entering water are per-
9 formed to study tsunamis generated by pyroclastic flows.
10 • In the near-field region, the wave features are mostly controlled by the mass flux
11 and the volume of the granular material, unlike the water depth.
12 • Beyond flow conditions, the grain size may affect the wave amplitude as it con-
13 trols the ability of water to penetrate the granular material.

Corresponding author: A. Bougouin, alexis.bougouin@uca.fr

Abstract

Novel laboratory experiments of fluidized granular flows entering water are reported, for the purpose of investigating tsunamis generated by pyroclastic flows. Qualitatively, the impact of a fluidized granular flow into water leads to (i) an initial vertical granular jet over water, (ii) a leading and largest wave, and (iii) a turbulent mixing zone forming a turbidity current. The present study focuses on the leading wave features in the near-field region, as a function of the mass flux per width q_m and the volume per width v of the flow, the maximum water depth H_o , and the slope angle θ of the inclined plane. The obtained waves are of Stokes and cnoidal types, for which the generation is mostly controlled by q_m and v . By contrast, H_o plays no role on the wave generation that occurs in the shallowest region. Moreover, a comparison between fluidized granular, dry (non-fluidized) granular, and water flows entering water is addressed under similar flow conditions. The dimensionless amplitude scales as $A/H_o = f(\zeta)$, where $\zeta = FrSM \sin \theta$ is a dimensionless parameter depending on the Froude number Fr , the relative slide thickness S , the relative mass M , and the slope angle θ . Data of fine fluidized granular, fine dry granular, and water flows collapse on a master curve, which implies that the nature of the flowing material is of lesser importance in the current setup. By contrast, coarse granular flows generate lower amplitude waves, which is attributed to the penetration of water into the porous granular medium.

Keywords: Tsunami, pyroclastic density current, fluidized granular flow.

1 Introduction

Tsunamis are long-period waves generated by a sudden displacement of the water surface, which can cause severe human and material damages near coastlines. A historical example is the earthquake-tsunami of December 2004 in Southeast Asia, killing more than 283,000 people on the coasts of the Indian Ocean (e.g., Lay et al., 2005). Although many tsunamis are triggered by submarine earthquakes, other mechanisms can also trigger these waves such as meteorite impacts (e.g., Wünnemann & Weiss, 2015), iceberg calvings (e.g., Heller et al., 2019), subaerial and submarine landslides (e.g., Harbitz et al., 2006; Løvholt et al., 2015), or volcanic eruptions (e.g., Paris, 2015). Despite this, tsunami risk assessments and warning systems are mainly structured to deal with earthquake-tsunamis, which make populations particularly vulnerable to other source mechanisms (Grezio et al., 2017). In particular, coastal communities living close to active volcanoes are commonly unprepared for tsunamis generated by underwater explosions, slope instabilities (submarine and subaerial landslides, flank collapses), caldera collapses, pyroclastic flows, or shock waves due to large explosions (Paris, 2015). However, volcanic tsunamis are not anecdotal phenomena as they cause about 20% of fatalities attributable to volcanic activities (Latter, 1981; Tanguy et al., 1998), even without taking into account the recent landslide-tsunami of December 2018 caused by the Anak Krakatau eruption (Indonesia) with a death toll of approximately 400 people (Grilli et al., 2019; Gouhier & Paris, 2019).

The entrance of pyroclastic flows into the sea has been reported as one of the major processes for the generation of volcanic tsunamis, that is, representing about 20% of recorded events (Paris, Switzer, et al., 2014). During the major Krakatau eruption of 1883, which killed more than 36,000 people on coastal areas around the Sunda Strait, a dozen tsunamis were observed (Verbeek, 1886). Four different scenarios have been suggested to explain these waves, namely, large flank collapses, submarine phreatomagmatic explosions, pyroclastic flows, or lateral blasts (Nomanbhoy & Satake, 1995; De Lange et al., 2001). Numerical models were compared to field data of the Tandjong Priok tide gauge at Batavia-Jakarta (Maeno & Imanura, 2011). The scenario of pyroclastic flows entering water led to better agreement than for the others, which is concordant with geological data (Carey et al., 2001; Paris, Wassmer, et al., 2014). It is now commonly accepted

65 that the impact of pyroclastic flows into the sea was the most likely source mechanism.
 66 In contrast, the waves recorded worldwide on maregrams were probably different from
 67 those observed in the Sunda Strait. A mechanism of long-period sea waves produced by
 68 phase coupling with atmospheric compressional gravity or shock waves has been proposed
 69 (Yokoyama, 1987). The tsunamis of the caldera-forming eruption of Santorini in the Late
 70 Bronze Age are also interpreted as a combination of pyroclastic flows reaching water and
 71 of slumping of submarine pyroclastic materials (Nomikou et al., 2016). Recently, sev-
 72 eral observations of tsunamis following the entrance of pyroclastic flows into the sea have
 73 been reported during the Rabaul 1994 eruption (Nishimura et al., 2005), the Montser-
 74 rat 1997 and 2003 eruptions (Pelinovsky et al., 2004; Mattioli et al., 2007), and the Strom-
 75 boli 2019 eruption. Despite this, the prediction of wave features in relation to pyroclas-
 76 tic flow conditions is poorly constrained due to a lack of knowledge on the dynamics of
 77 pyroclastic flows and their interaction with water. Moreover, experimental, numerical,
 78 and theoretical studies, which consider the specific case of pyroclastic flows entering wa-
 79 ter, are limited and rarely focused on the wave generation. For instance, Freundt (2003)
 80 and Allen et al. (2012) investigated experimentally the emplacements and deposits of hot
 81 volcanic tephra flows entering water, while Watts and Waythomas (2003) proposed a the-
 82 oretical analysis on tsunami features generated by pyroclastic density currents by tak-
 83 ing into account both the upper dilute suspension and basal dense flow. Finally, these
 84 works mainly addressed thermal effects, disregarding the high pore fluid pressure of such
 85 flows raised in this study.

86 The present study aims to investigate the generation of tsunamis by pyroclastic flows
 87 during explosive volcanic eruptions. In this objective, novel laboratory experiments of
 88 fluidized granular flows entering water are addressed. This simplified configuration en-
 89 sures a suitable modeling of concentrated pyroclastic flows reaching the sea, consider-
 90 ing both the high mobility and the interstitial gas pore pressure of these flows. The present
 91 work focuses on the characterization of the leading and largest wave by varying the mass
 92 flux per width q_m and the volume per width v of the granular flow, the maximum wa-
 93 ter depth H_o , and the slope angle θ of the inclined plane. The paper is organized as fol-
 94 lows. In section 2, earlier works on this issue are presented. Then, the experimental setup
 95 is described (section 3). In section 4, preliminary observations of a fluidized granular flow
 96 entering water are reported and the control parameters are discussed. Finally, the lead-
 97 ing wave is analyzed in terms of different parameters (section 5) and a comparison be-
 98 tween fluidized granular, dry (nonfluidized) granular, and water flows entering water is
 99 done (section 6).

100 2 Earlier works

101 To improve the understanding of tsunamis induced by the impact of a subaerial
 102 flow, several canonical configurations have been investigated through theoretical mod-
 103 els, laboratory experiments, and numerical simulations. Overall, two specific configura-
 104 tions can be distinguished, namely, the entrance of a solid block (piston model, block falling
 105 vertically or sliding down an inclined plane) or of a fluid-like material (Newtonian fluid,
 106 granular mass, grain-liquid mixture) into water. In the following, earlier studies consid-
 107 ering a mass initially above the water surface will be presented and other configurations
 108 of fully or partially immersed slides will be disregarded (see Løvholt et al., 2015; Yavari-
 109 Ramshe & Ataie-Ashtiani, 2016, and references herein for more details).

110 Early studies focused on the most simplified configuration of a solid block impact-
 111 ing water. Depending on initial conditions, a wide range of wave types were observed,
 112 such as Stokes waves, cnoidal waves, solitary waves, and bores (e.g., Heinrich, 1992; Heller
 113 & Spinneken, 2015). A classification has been proposed using the wave features (Le Méhauté,
 114 1976) or the slide parameters (Fritz et al., 2004; Heller & Hager, 2011; Heller & Spin-
 115 neken, 2015). In the case of a 2D geometry, the leading wave is usually the most signif-
 116 icant wave containing the major part of the energy transferred at the impact, which could

117 be then affected by the dispersion (Law & Brebner, 1968). Its features depend on the
 118 impact velocity, the geometry and mass of the slide block, the inclination angle of the
 119 plane, and the water depth (Law & Brebner, 1968; Kamphuis & Bowering, 1970; Mon-
 120 aghan et al., 2003; Walder et al., 2003; Viroulet et al., 2013). However, the modeling of
 121 tsunamis by solid blocks in the context of waves triggered by granular flows has impor-
 122 tant limitations (Heller & Kinnear, 2010; Yavari-Ramshe & Ataie-Ashtiani, 2016). For
 123 example, the deformation and the permeability of the granular material could affect the
 124 wave characteristics (Lindstrøm, 2016). Usually, the amplitude and the period of the lead-
 125 ing wave are reduced and increased, respectively, for granular materials compared to solid
 126 blocks with the same initial conditions (Ataie-Ashtiani & Nik-Khah, 2008; Heller & Kin-
 127 near, 2010).

A more realistic modelling of natural granular flows is the release of a granular mass on an inclined plane. In this case, dimensionless parameters governing the generation of waves are the Froude number $Fr = u_s/(gH_o)^{1/2}$, the relative slide thickness $S = h_s/H_o$, and the relative slide mass $M = \rho v/\rho_f H_o^2$, where u_s , h_s , ρ , and v are the velocity, the thickness, the bulk density, and the volume per width (i.e., the area orthogonal to the spanwise direction) of the granular flow, ρ_f is the water density, H_o is the maximum water depth, and g is the gravitational acceleration. Depending on Fr and S , Fritz et al. (2003b) reported different dynamics of the granular flow and of the leading wave at the impact. For large Fr and S , the water was ejected upward forming an air cavity behind the flow front. In contrast, for lower Fr and S , the height profile was shaped by water. Moreover, Fritz et al. (2004) reported an empirical equation depending on both Fr and S to predict the maximum amplitude of the generated wave. Zweifel et al. (2006) gave an empirical relation including the relative mass M in addition to the Froude number Fr and the relative slide thickness S . Finally, Heller and Hager (2010) proposed an empirical impulse product parameter to predict the wave characteristics (e.g., amplitude, height, wavelength, and period) as

$$P = FrS^{1/2}M^{1/4}\cos^{1/2}\left(\frac{6\theta}{7}\right), \quad (1)$$

128 which is related to the streamwise slide momentum flux component. In the three-dimensional
 129 configuration, it has been supported that the Froude number is also the dominant di-
 130 mensionless parameter in the wave generation (Mohammed & Fritz, 2012). However, the
 131 use of P led to an important inaccuracy on the wave features, used in the case of neg-
 132 atively buoyant granular flows (Heller & Hager, 2010; Miller et al., 2017), positively buoy-
 133 ant granular flows (Zitti et al., 2016), and water flows (Bullard, Mulligan, Carreira, &
 134 Take, 2019). For example, Heller and Hager (2010) concluded to an inaccuracy up to $\pm 30\%$
 135 on the relative maximum amplitude and to $\pm 50\%$ on the relative wave period.

136 Although a granular material is relevant for modeling rock avalanches, it is limited
 137 in the case of pyroclastic density currents. Indeed, these gravity-driven hot gas-particle
 138 flows are usually composed of an upper dilute turbulent suspension, often referred to as
 139 pyroclastic surge, and a basal concentrated granular avalanche, called pyroclastic flow
 140 (Dufek, 2016). While the dilute region can be modeled as a turbulent gravity current,
 141 the basal region is more difficult to describe. In particular, pyroclastic flows commonly
 142 travel on gentle slopes over distances of several kilometers to several tens of kilometers
 143 at speeds of up to about a hundred kilometers per hour, which set them apart from dry
 144 granular flows. Sparks (1976) and Wilson (1980) first proposed that the high mobility
 145 of these flows was due to their high interstitial gas pore pressure. The sustained pore pres-
 146 sure, which may arise if the permeability is small owing to large amounts of fine ash, con-
 147 terbalances the weight of grains and therefore reduces the internal friction. In this con-
 148 text, the fluidization process and related pore pressure effect have been studied intensi-
 149 vely (e.g., Roche et al., 2002; Dufek & Manga, 2008; Girolami et al., 2008; Montser-
 150 rat et al., 2012; Rowley et al., 2014; Valverde & Soria-Hoyo, 2015; Chédeville & Roche,
 151 2014; Chédeville & Roche, 2018; Breard et al., 2018; Smith et al., 2018; Lube et al., 2019;

152 Soria-Hoyo et al., 2019). At the laboratory scale, if the pore pressure is maintained long
 153 enough owing to slow pressure diffusion, the dynamics of a fluidized granular flow is simi-
 154 lar to that of the well-known dam-break flow of pure fluids for which energy dissipation
 155 is weak (Roche et al., 2008). At longer times when pore pressure has diffused, the granu-
 156 lar material is defluidized, decelerates, and can stop, at sufficiently low slopes. In this
 157 case, the final deposit is elongated with a runout length significantly larger than that of
 158 an equivalent dry granular flow (Roche et al., 2011). In the present study, granular flows
 159 with sustained high gas pore pressure are considered to ensure the dynamic similarity
 160 with natural pyroclastic flows.

161 3 Methodology

162 3.1 Experimental setup

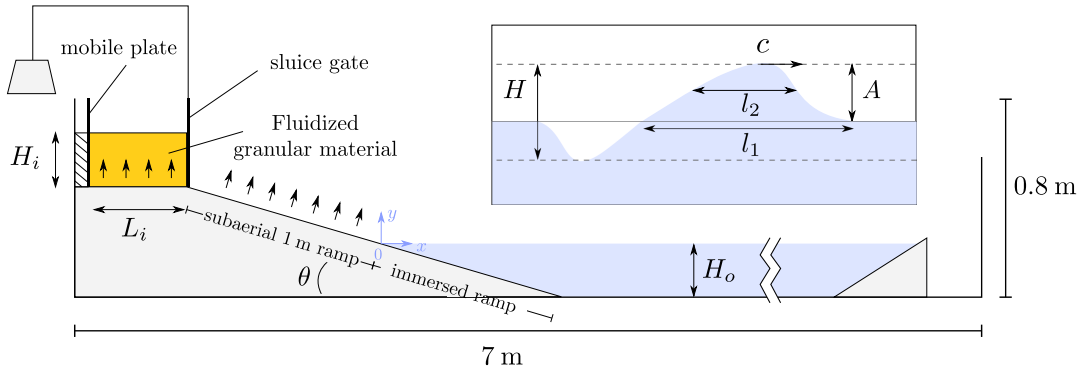


Figure 1. Sketch of the experimental apparatus with the initial parameters (height H_i and length L_i of the initial column of grains, slope angle θ and maximum water depth H_o) and the wave features (crest velocity c , amplitude A , height H , crest length l_1 and half-amplitude length l_2). Black arrows represent the air flux perpendicular to the bottom for the fluidization process.

163 The experimental setup consists in a horizontal transparent channel of rectangular-
 164 cross section with dimensions of 7 m long, 0.8 m high and 0.2 m wide along the stream-
 165 wise x , vertical y , and spanwise z coordinates, respectively (see Figure 1). The origin
 166 of the coordinate system (x, y) is located at the shoreline, defined as the position where
 167 the undisturbed water surface crosses the inclined plane. On one side, the channel is equipped
 168 with a finite volume reservoir delimited by a sluice gate and a mobile vertical plate. The
 169 initial column of the flowing material is defined by its length and its height, which are
 170 varied in the range $L_i = [8.5 : 33.8] \pm 0.1$ cm and $H_i = [10 : 79.5] \pm 0.5$ cm, respec-
 171 tively. The reservoir is connected to an inclined plane with a slope angle of $\theta = 5^\circ, 10^\circ,$
 172 $15^\circ,$ or 20° . In this paper, most of the results correspond to experiments performed with
 173 $\theta = 15^\circ$. The inclined plane is splitted into a subaerial 1 m and an immersed ramp. The
 174 latter one ranges from 0.38 m to 1.5 m, with the maximum water depth varied in the
 175 range $H_o = [13.1 : 38.5] \pm 0.1$ cm. Both the reservoir and the subaerial ramp are equipped
 176 with a porous plate to fluidize the granular material by an air flux perpendicular to the
 177 bottom (see arrows in Figure 1). At the end of the channel, an inclined plate followed
 178 by a void volume limits the reflected waves.

179 At the initial time of the experiment (i.e., $t = 0$), the sluice gate is removed at
 180 about a constant speed of $2 \text{ m}\cdot\text{s}^{-1}$, by releasing a suspended weight. The dynamics of
 181 the granular flow and of the disturbed water surface are extracted from image analysis
 182 using a classical shadowgraphy method. The free surface is distinguished from the am-

183 bient air, by addition of a red dye into water. Two Photron Fastcam 1024×1024 pixel
 184 cameras and LED panels on the opposite side of the channel are used. In the stream-
 185 wise direction, the two cameras are located at $x = 1$ m and $x = 2.4$ m from the shore-
 186 line, respectively. In the vertical direction, the cameras are located at the same level as
 187 the undisturbed initial water surface to prevent image distortion. For the second cam-
 188 era, a light signal turns off at the opening of the sluice gate to determine the initial time.
 189 The acquisition rate is 250 Hz and the spatial resolution is 4 mm/pixel and 0.8 mm/pixel,
 190 respectively. The high-resolved and more distant camera, for which the field of view is
 191 included in that of the large view camera, aims to obtain a better accuracy of wave fea-
 192 tures. Finally, the extraction process is performed using a Matlab routine, based on a
 193 threshold method.

194 3.2 Materials

195 The granular material used corresponds to monodisperse spherical glass beads man-
 196 ufactured by Wheelabrator. The diameter and density of beads are measured as $d =$
 197 $65 \pm 10 \mu\text{m}$ and $\rho_p = 2550 \pm 50 \text{ kg.m}^{-3}$, respectively. The angle of avalanche α_a and
 198 the angle of repose α_r are also estimated from the variations of the slope of an initially
 199 horizontal plane granular bed in a transparent box ($5 \times 11 \times 18 \text{ cm}^3$) which is slowly
 200 tilted. The angle of avalanche is the critical angle above which grains spontaneously starts
 201 to flow, until the granular material stabilizes at the angle of repose. Here, they are equal
 202 to $\alpha_r = 25 \pm 1^\circ$ and $\alpha_a = 29 \pm 1^\circ$, respectively. It can be noted that the slope angle θ
 203 of the inclined plane is always lower than the repose angle α_r of the granular material.
 204 It means that, for dry (nonfluidized) granular collapses, the mass does not entirely enter
 205 water and a final deposit formed on the subaerial ramp, unlike fluidized granular flows
 206 (Bougouin et al., 2019). The case of fluidized granular flows allows therefore to inves-
 207 tigate lower slope angles with an entire mobility of the granular mass compared to the
 208 analogous dry situation. Finally, the initial volume fraction of the granular column is $\phi_i \sim$
 209 0.56 ± 0.01 .

210 Some experiments with salt water flows have also been performed, in order to com-
 211 pare the results with fluidized and dry granular flows. In this case, sodium chloride (NaCl)
 212 is added in dyed water with a concentration of 325 g/kg of water, giving a salt water flow
 213 denser than the fresh water in the channel. The obtained density is $\rho = 1197 \text{ kg.m}^{-3}$
 214 measured by a DMA 35 Anton Paar electronic densimeter with an accuracy of $\pm 0.5 \text{ kg.m}^{-3}$.

215 3.3 Laboratory modeling of pyroclastic flows

216 In the present study, a specific attention is paid on the modeling of pyroclastic den-
 217 sity currents at the laboratory scale. In particular, the basal concentrated flow is only
 218 considered here, as it mainly contributes in the wave generation (Watts & Waythomas,
 219 2003). A suitable modeling of natural pyroclastic flows with large amounts of ash con-
 220 ferring a low material permeability corresponds to fluidized granular flows (Roche, 2012).
 221 The fluidization process generates high pore fluid pressure, which reduces the internal
 222 friction and therefore promotes the high mobility (e.g., long runout distance). In this study,
 223 the minimum fluidization velocity of the granular material is $U_{mf} \sim 3.8 \text{ mm.s}^{-1}$, es-
 224 timated as the velocity for which the gas pore pressure counterbalances the pressure of
 225 a static granular column. Before each experiment, the granular material is fluidized and
 226 the air flow rate is then switched off. This process leads to a dilatation of the granular
 227 column, which allows to obtain an equivalent initial volume fraction $\phi_i \sim 0.56 \pm 0.01$,
 228 for dry and fluidized granular materials. In the latter case, the granular material is re-
 229 fluidized with an air velocity of $U_f = 4.7 \pm 0.1 \text{ mm.s}^{-1}$, without significant decompaction,
 230 which ensures a fully fluidized flow, that is, $U_f/U_{mf} \sim 1.2 > 1$. Additionally, the pres-
 231 sure diffusion of natural flows is relatively slower than at the laboratory scale essentially
 232 because of flow thickness (Rowley et al., 2014; Smith et al., 2018). The granular mate-
 233 rial is therefore fully fluidized until it reaches water, both in the reservoir and on the sub-

234 aerial inclined plane. Note that, other specific features of pyroclastic flows, such as heat
 235 transfers, are disregarded (see Freundt, 2003; Allen et al., 2012, for some details on ther-
 236 mal effects).

237 A posteriori of experiments, the dynamics of fluidized granular flows can be quan-
 238 tified by the flow Froude number defined as $Fr^f = u_f / (gh_f)^{1/2}$, where u_f and h_f are
 239 the velocity and the height at the front (u_f and h_f will be defined later in section 4.2).
 240 In the present study, this dimensionless parameter is found in the range $Fr^f = [6 : 9]$,
 241 which is in the upper range given for natural pyroclastic flows $Fr^f = [10^{-1} : 10^1]$ (Freundt,
 242 2003; Roche, 2012; Delannay et al., 2017). Additionally, the bulk flow to water density
 243 ratio ρ/ρ_f can be estimated, being an important parameter in the wave generation. In
 244 the case of granular flows, the bulk density is defined as $\rho = \phi\rho_p + (1 - \phi)\rho_a$, where ϕ
 245 is the volume fraction of grains, and $\rho_p = 2550 \text{ kg.m}^{-3}$ and $\rho_a = 1.2 \text{ kg.m}^{-3}$ are the
 246 grain and ambient air densities. In the current setup, the volume fraction ϕ at the im-
 247 pact cannot be measured. In our experiments and in the analysis below, it is therefore
 248 assumed that the fluidization maintains the volume fraction from the initial state to the
 249 impact, $\phi = \phi_i \sim 0.56 \pm 0.01$. By contrast, for the dry granular configuration, it is
 250 probable that a slight compaction occurs as $\phi \sim 0.58 - 0.59$, corresponding to the crit-
 251 ical volume fraction for which no contraction or dilatation are necessary to flow on gen-
 252 tle slopes (Pouliquen, 1999; Gravish & Goldman, 2014). The bulk density of fluidized
 253 granular flows is therefore equal to $\rho \sim 1400 \text{ kg.m}^{-3}$, leading to $\rho/\rho_f \sim 1.4$ included
 254 in the upper range estimated for pyroclastic flows $\rho/\rho_f = [0.05 : 1.5]$ (Freundt, 2003;
 255 Roche, 2012; Delannay et al., 2017). To conclude, the present study mainly focuses on
 256 the modeling of the denser and faster pyroclastic flows entering the sea.

257 4 Laboratory experiments of a fluidized granular flow into water

258 4.1 Preliminary observations

259 In Figure 2, the typical evolution of a fluidized granular flow entering water is shown,
 260 at five different times. A movie of the same experiment is also available in the Support-
 261 ing Information. After the release of the initial column, the fluidized granular material
 262 accelerates on the inclined plane until it reaches a constant front-velocity. Then, the gran-
 263 ular flow impacts water, leading first to a single vertical granular jet over water (Figure
 264 2a). This behavior has already been reported for the entrance of experimental volcanic
 265 ash flows into water (Freundt, 2003), while it has never been observed for coarse grains
 266 $d > \mathcal{O}(10^{-3}) \text{ m}$ (Fritz et al., 2003a; Viroulet et al., 2014; Miller et al., 2017). The ver-
 267 tical jet is also obtained in the case of salt water flows impacting water. Simultaneously,
 268 the granular material pushes water, and it generates a large-amplitude wave, which can
 269 be followed by low-amplitude waves. The wave breaks quickly after the impact, and grains,
 270 previously ejected by the initial jet, fall onto it. The grains are mixed and partially trans-
 271 ported by the breaking wave before they settle into water (Figures 2b and 2c). Surpris-
 272 ingly, the amplitude A of the leading and largest wave is much larger than the flow thick-
 273 ness h_f ($A/h_f \sim 8$ for this experiment). Additionally, the entrance of the granular ma-
 274 terial into water leads to a turbulent mixing zone with a roughly linear interface to clear
 275 water (Figure 2b). Then, a turbidity current emerges from the mixing zone on the im-
 276 mersed inclined plane (Figure 2c). Indeed, this current behaves like a particle-laden grav-
 277 ity current in which grains are mainly suspended by the turbulent fluid (e.g., Kneller &
 278 Buckee, 2000). At early times of its propagation, a lot of bubbles, originating probably
 279 to the interstitial gas of the flow, are released. The turbidity current propagates until
 280 the end of the channel (Figures 2d and 2e). In the range of parameters considered, the
 281 wave velocity is always faster than that of the turbidity current, with about a factor 4.
 282 Finally, a thick granular deposit is obtained at the end of the immersed inclined plane
 283 (not shown here), which suggests a significant settling of particles at the impact. Note
 284 that the flow dynamics and the final deposit of the granular material beneath the wa-
 285 ter surface are disregarded in the present study.

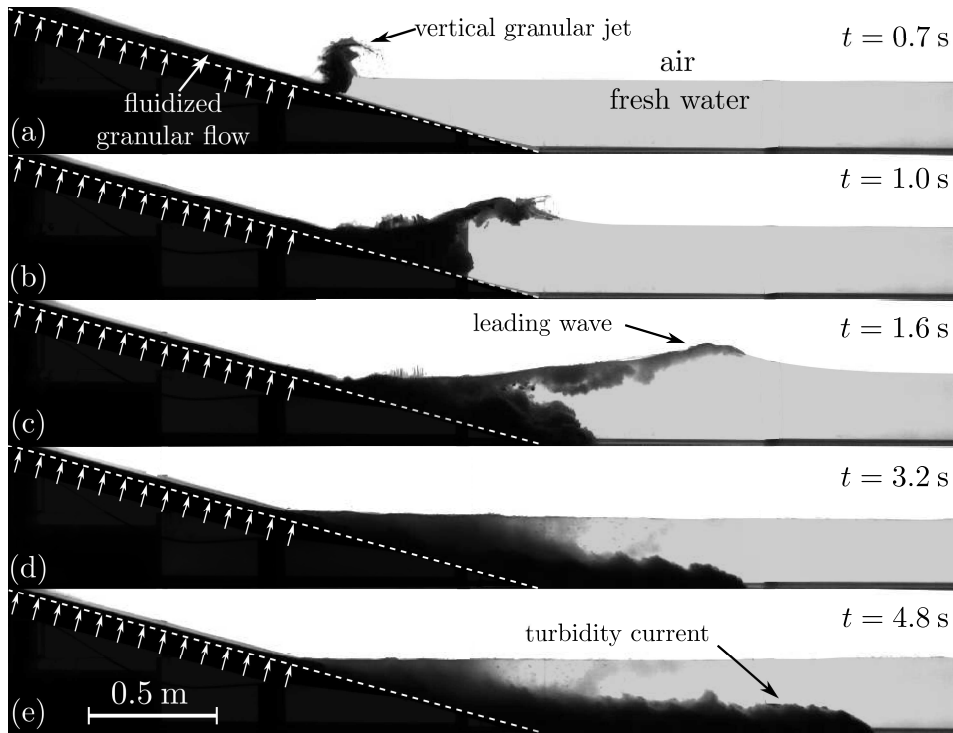


Figure 2. Snapshots of a fluidized granular flow entering water, at five different times, after gate opening at $t = 0$. The initial conditions are $H_i = 21.5$ cm, $L_i = 33.8$ cm, $\theta = 15^\circ$, and $H_o = 26.5$ cm. White arrows represent the air flux perpendicular to the inclined plane for the fluidization process.

286

4.2 Control parameters

287

288

289

290

291

292

293

294

In view of these preliminary observations and of earlier works, it is relevant to define the control parameters at the impact. In particular, the fluidized granular flow can be characterized by its constant front-velocity u_f and its front-height h_f , its volume per width v and its bulk flow density ρ . As discussed in section 3.3, the bulk flow density, defined as $\rho = \phi_i \rho_p + (1 - \phi_i) \rho_a$, is roughly constant in the set of experiments. However, the volume per width v is dependent on the characteristic lengths of the initial column, while the dependency of u_f and h_f on initial parameters is not trivial. In the Supporting Information, a summary table of control parameters is provided (Table S1).

295

296

297

298

299

300

301

302

303

304

305

306

Figure 3 presents (a) the constant flow front-velocity u_f and (b) the front-height h_f at the impact, as a function of the initial height H_i of the granular column, with $\theta = 15^\circ$. In this study, the front-height h_f is defined as the flow height at 10 cm behind the front to prevent the important gradient of the height profile, while remaining relatively close to the front (more details are provided in the Supporting Information). Moreover, the length of the initial column varies here, but no effect on u_f and on h_f has been observed. Indeed, it has already been reported that u_f is mostly controlled by the initial height H_i of the column in the case of dry granular collapses over inclined planes (Farin et al., 2014) and of fluidized granular flows on horizontal planes (Roche et al., 2008). Finally, the lower and upper horizontal error bars correspond to the values of $H_i - h_r$ and H_i , respectively, where $h_r \sim 3$ cm is the height of the granular mass remaining in the reservoir at the end of the experiment.

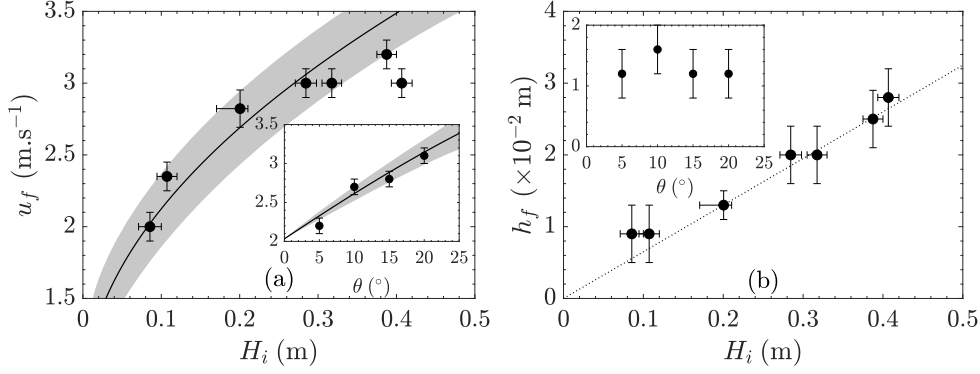


Figure 3. (a) Constant flow front-velocity u_f and (b) front-height h_f at the impact, as a function of the initial height H_i of the granular column, with $\theta = 15^\circ$. The insets represent u_f and h_f as a function of the slope angle θ , with $H_i = 21.5$ cm and $L_i = 33.8$ cm. (—) Equation (2) with $\beta = 1.4$ and $t = T = 0.3$ s (inset: $t = T = 0.35$ s), where T is the flow time to reach the constant-front velocity u_f after the experiments. The gray area shows the scatter of T in the range ± 0.1 s (inset: ± 0.05 s). (\cdots) $h_f^{(s)}/H_i = 6.5\%$.

307 Both the constant-front velocity u_f (Figure 3a) and the front-height h_f (Figure 3b)
 308 are shown to increase for increasing H_i . For $H_i > 0.25$ m, it seems that u_f becomes
 309 constant, but there is no physical explanation and further experiments will therefore be
 310 necessary to support this trend. The front-height h_f evolves linearly with H_i , with in
 311 particular $h_f^{(s)}/H_i = 6.5\%$ (dotted line, in Figure 3b). Additionally, the insets show u_f
 312 and h_f as a function of the slope angle θ , for $H_i = 21.5$ cm and $L_i = 33.8$ cm. The
 313 front-velocity u_f increases for increasing θ , similar to granular collapses over inclined planes
 314 (Mangeny et al., 2010). In contrast, the front-height h_f is not affected by the slope angle
 315 θ and a constant mean value $h_f \sim 1.2$ cm is obtained here.

For a sudden release of a finite volume of frictionless fluid down an inclined plane,
 well-known as the dam-break problem, shallow-water equations can be used to predict
 the flow front-velocity (Ancey et al., 2008, and references herein). It is obtained

$$u_f^{th} = \beta \sqrt{gH_i \cos \theta} + gt \sin \theta, \quad (2)$$

316 where the constant parameter $\beta = 2$ theoretically. In the horizontal case (i.e., $\theta = 0^\circ$),
 317 the Ritter analytical solution is also recovered, which predicts a constant front-velocity
 318 $u_f^{th} = 2\sqrt{gH_i}$ for a semi-infinite volume (Ritter, 1892). For the inclined configuration,
 319 equation (2) predicts a constant acceleration of the flow as $du_f^{th}/dt = g \sin \theta$. In our ex-
 320 periments, acceleration is only observed up to $t = T \sim 0.3 \pm 0.1$, above which the front-
 321 velocity becomes constant. This difference could be attributed to the hypothesis of the
 322 model, in particular, that the solid bottom and wall friction are neglected. In the fol-
 323 lowing, it is assumed that equation (2) is applicable up to $t = T$, and the constant front-
 324 velocity u_f can be estimated, at $t = T$, with β a fitting parameter.

325 In Figure 3a, the solid line represents the analytical solution of dam-break flows
 326 over an inclined plane u_f^{th} (equation (2)) with $\beta = 1.4$ and $t = T = 0.3$ s. The gray
 327 area indicates the scatter of T in the range ± 0.1 s, after the experiments. The general
 328 trend of both the analytical solution and the experimental data are in good agreement.
 329 Additionally, in the case of dam-break flows on a horizontal plane, it is well known that
 330 a value of $\beta = 2$ is hardly reached due to bottom shear dissipation, which becomes sig-
 331 nificant in regions where the depth of the current becomes small, particularly close to
 332 the front (Dressler, 1952; Hogg & Woods, 2001; Hogg & Pritchard, 2004). In the liter-

333 ature, the parameter β is usually found in the range $\beta = [1 : 2]$ (Dressler, 1954; Jánosi
 334 et al., 2004; Leal et al., 2006; Roche et al., 2008; Bonometti et al., 2008; Bouguin et al.,
 335 2017), according to the value $\beta = 1.4$ obtained here. Similar conclusions can be drawn
 336 from the inset of Figure 3a. The experimental data and equation (2), with $\beta = 1.4$ and
 337 $t = T = 0.35 \pm 0.05$ s, match very well together.

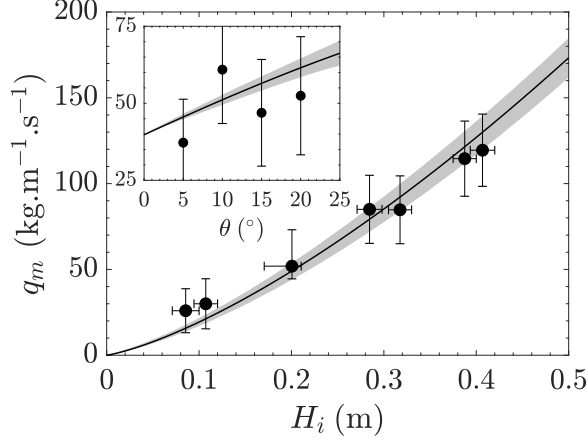


Figure 4. Mass flux per width $q_m = \rho u_f h_f$ at the impact, as a function of the initial height H_i of the granular column, with $\theta = 15^\circ$. The inset shows q_m as a function of the slope angle θ , with $H_i = 21.5$ cm and $L_i = 33.8$ cm. (—) predictive model $q_m^{(s)} = \rho u_f^{th} h_f^{(s)}$, where $\rho = 1400$ kg.m⁻³, u_f^{th} defined by equation (2) with $\beta = 1.4$ and $t = T = 0.3$ s (inset: $t = T = 0.35$ s), and $h_f^{(s)}/H_i = 6.5\%$ (dotted line, in Figure 3b). The gray area shows the scatter of T in the range ± 0.1 s (inset: ± 0.05 s).

338 For θ fixed, the constant flow front-velocity u_f and the front-height h_f increase to-
 339 gether for increasing H_i . Thus, it is not possible to vary these two parameters indepen-
 340 dently. In this way, the mass flux per width $q_m = \rho u_f h_f$ is defined, including both the
 341 velocity u_f and the height h_f of the granular flow. As expected, q_m increases for increas-
 342 ing H_i and θ , as shown in Figure 4. In the latter case, the increase of q_m is only due to
 343 the θ -dependency of u_f , while h_f is not affected. Moreover, the predictive model $q_m^{(s)} =$
 344 $\rho u_f^{th} h_f^{(s)}$ (solid line and gray area) is in fairly good agreement with the experimental data
 345 with a similar trend.

346 5 Characterization of the leading wave

347 In this section, the leading and largest wave features are analyzed in light of the
 348 mass flux per width $q_m = \rho u_f h_f$ and the volume per width $v = (H_i - h_r)L_i$ of the
 349 granular flow, with $h_r \sim 3$ cm the height of the granular mass remaining into the reser-
 350 voir at the end of the experiment, and the maximum water depth H_o . The wave is de-
 351 fined by its amplitude A , its height H , its crest length l_1 , its half-amplitude length l_2 ,
 352 and its crest velocity c (see Figure 1). Note that the amplitude of the leading and largest
 353 wave at $x = 2, 2.4$ and 2.8 m from the shoreline, is provided in the summary table in
 354 the Supporting Information (Table S1).

355 5.1 Wave types

356 Figure 5 presents a diagram of wave types in the $(H_o/gT^2, H/gT^2)$ plane, based
 357 on Le Méhauté (1976). In particular, regions of linear, Stokes, and cnoidal waves are in-

358 dicated with colored areas. Experimental data of the present study are also represented,
 359 corresponding to the wave features at $x = 2$ m (circles), $x = 2.4$ m (squares) and $x =$
 360 2.8 m (diamonds) from the shoreline. The period of the leading wave is defined as $T =$
 361 $2l_1/c$.

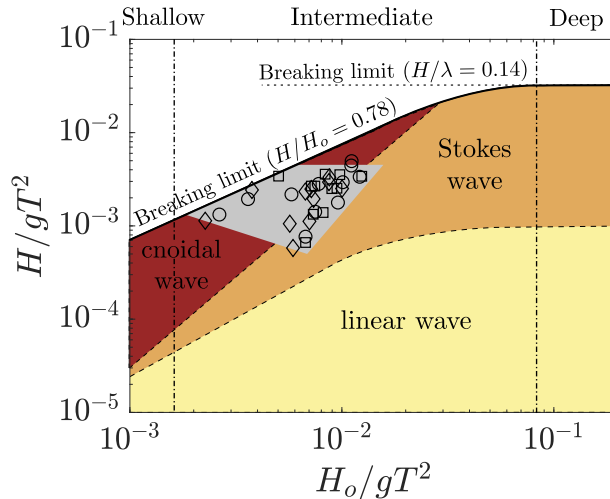


Figure 5. Diagram of wave types in the $(H_o/gT^2, H/gT^2)$ plane, based on Le Méhauté (1976). Experimental data of the present study are also represented with $T = 2l_1/c$ the period of the leading and largest wave, at $x = 2$ m (circles), $x = 2.4$ m (squares) and $x = 2.8$ m (diamonds) from the shoreline. Gray area represents the range of the experiments performed in this study.

362 The diagram is limited by a breaking criterion above which wave breaking occurs
 363 (solid line in Figure 5). In shallow and deep water conditions, this criterion reduces to
 364 $H/H_o = 0.78$ (McCowan, 1894) and $H/\lambda = 0.14$ (Michell, 1893), respectively. In the
 365 present study, all experiments are below the breaking criterion, which suggests that most
 366 of leading waves have probably already broken. Note that wave breaking is expected to
 367 occur for lower H/H_o , given that the wave generation takes part in the shallow region
 368 of the inclined plane (more discussed in section 5.3). Secondly, all experiments performed
 369 here corresponds to Stokes and cnoidal wave types, while some data are broadly close
 370 to the Stokes-cnoidal transition. The diagram provides merely a qualitative representa-
 371 tion of wave type regions and caution must be exercised with these transitions. Finally,
 372 all experiments correspond to the intermediate water depth conditions, similar to waves
 373 generated by a pneumatic granular flow generator (Fritz et al., 2004). Remind that ro-
 374 bust wave theories are mainly available for linear waves, for Stokes waves in deep wa-
 375 ter, and for cnoidal waves in shallow water, under steady-state conditions. In our case,
 376 there are therefore no applicable water wave theories.

377 5.2 Role of the granular flow: mass flux and volume

378 Figure 6 presents the temporal evolution of the water height profile η for different
 379 mass fluxes per width q_m and different volumes per width v of the granular flow. More
 380 specifically, the influence of q_m (Figures 6a and 6b) and v (Figures 6c and 6d) on the
 381 leading and largest wave is shown, while other parameters are kept constant.

382 No perturbation is observed as long as the leading wave has not reached the most
 383 proximal wave gauge location, at $t \sim 1.5$ s. For $t \gtrsim 1.5$ s, the water surface is disturbed
 384 with a first positive crest which is also the largest one. At low q_m and v (Figures 6a and

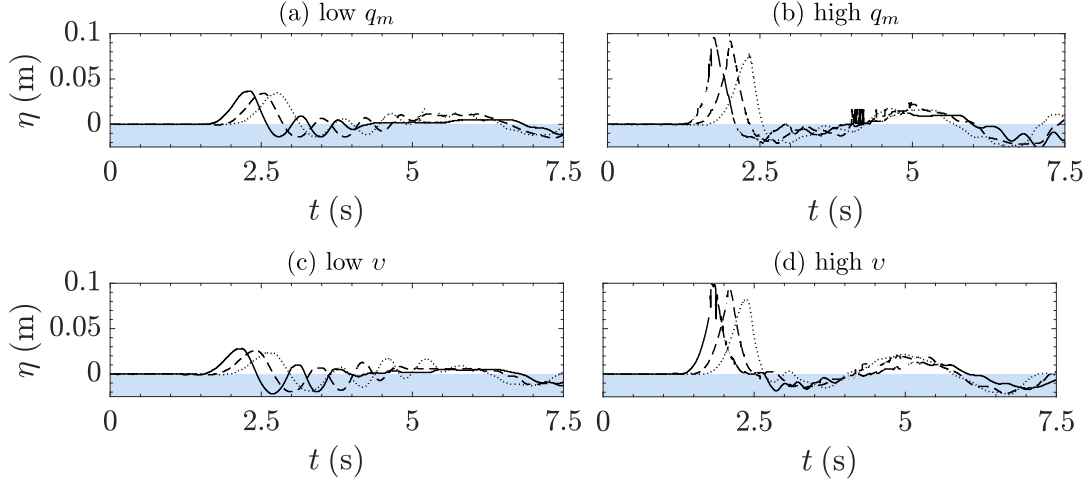


Figure 6. Temporal evolution of the water height profile η for (a) $q_m = 30 \text{ kg}\cdot\text{m}^{-1}\cdot\text{s}^{-1}$, $v = 3.1 \text{ dm}^2$, (b) $q_m = 115 \text{ kg}\cdot\text{m}^{-1}\cdot\text{s}^{-1}$, $v = 3.1 \text{ dm}^2$, (c) $q_m = 45 \text{ kg}\cdot\text{m}^{-1}\cdot\text{s}^{-1}$, $v = 1.5 \text{ dm}^2$, and (d) $q_m = 47 \text{ kg}\cdot\text{m}^{-1}\cdot\text{s}^{-1}$, $v = 6.3 \text{ dm}^2$, at (—) $x = 2 \text{ m}$, (---) $x = 2.4 \text{ m}$ and (\cdots) $x = 2.8 \text{ m}$ from the shoreline, with $\theta = 15^\circ$ and $H_o = 26.5 \text{ cm}$.

385 6c), the leading wave is followed by low-amplitude waves, while only a single large-amplitude
 386 wave is obtained at large q_m and v (Figures 6b and 6d). Note that, in Figures 6b and
 387 6d, the elevation of the free-surface, at $t \sim 5 \text{ s}$, is attributed to a part of the leading
 388 wave reflected by the wave breaker. Moreover, the effect of q_m and of v on the water sur-
 389 face is very similar. At low q_m and v , the leading and largest wave is smooth and slightly
 390 nonlinear with a moderate amplitude $A \sim 3.5 \text{ cm}$ (Figure 6a) and $A \sim 2.3 - 2.8 \text{ cm}$
 391 (Figure 6c). By contrast, at large q_m and v , the wave is strongly nonlinear with a trough
 392 much smaller than the steep crest. The wave amplitude is larger than at low q_m and v ,
 393 with in particular, $A \sim 7.9 - 9.6 \text{ cm}$ (Figure 6b) and $A \sim 8.1 - 10.0 \text{ cm}$ (Figure 6d).
 394 In both cases, the amplitude A decreases during the wave propagation from $x = 2 \text{ m}$
 395 to $x = 2.8 \text{ m}$ from the shoreline.

396 Figure 7 shows (a,b) the amplitude A and (c,d) the crest length l_1 of the leading
 397 and largest wave as a function of (a,c) the mass flux per width q_m and (b,d) the volume
 398 per width v of the granular flow, at three different positions from the shoreline. As ex-
 399 pected, the wave amplitude A increases for increasing q_m and v (Figure 7a and 7b). In
 400 particular, A increases by a factor 2.5 and 3.5 when q_m and v are increased by a factor
 401 4, respectively. Similar conclusions can be drawn from the evolution of the wave height
 402 H with q_m and v (insets of Figures 7a and 7b). The influence of q_m and v on the wave
 403 amplitude are therefore of the same order of magnitude. Additionally, H seems to reach
 404 a constant value $H \sim 0.1 \text{ m}$, for $v \gtrsim 4.7 \text{ dm}^2$ (inset of Figure 7b). It suggests that,
 405 at sufficiently large v , the volume of the granular flow should not affect the wave gen-
 406 eration. More specifically, if the flow duration is much longer than the wave generation,
 407 it is expected that the finite volume does not play a role on the wave features, and the
 408 problem can be related to an infinite volume entering water. In our experiments, the wave
 409 features are still affected by the granular volume per width v , knowing that the genera-
 410 tion occurs in less than 0.5 s , as discussed later in section 5.3. Finally, the amplitude
 411 A is shown to decrease significantly during the propagation of the leading wave, from
 412 $x = 2 \text{ m}$ (solid lines with circles) to $x = 2.8 \text{ m}$ (dotted lines with diamonds) from the
 413 shoreline. This decrease is much less pronounced for the wave height H . During the wave

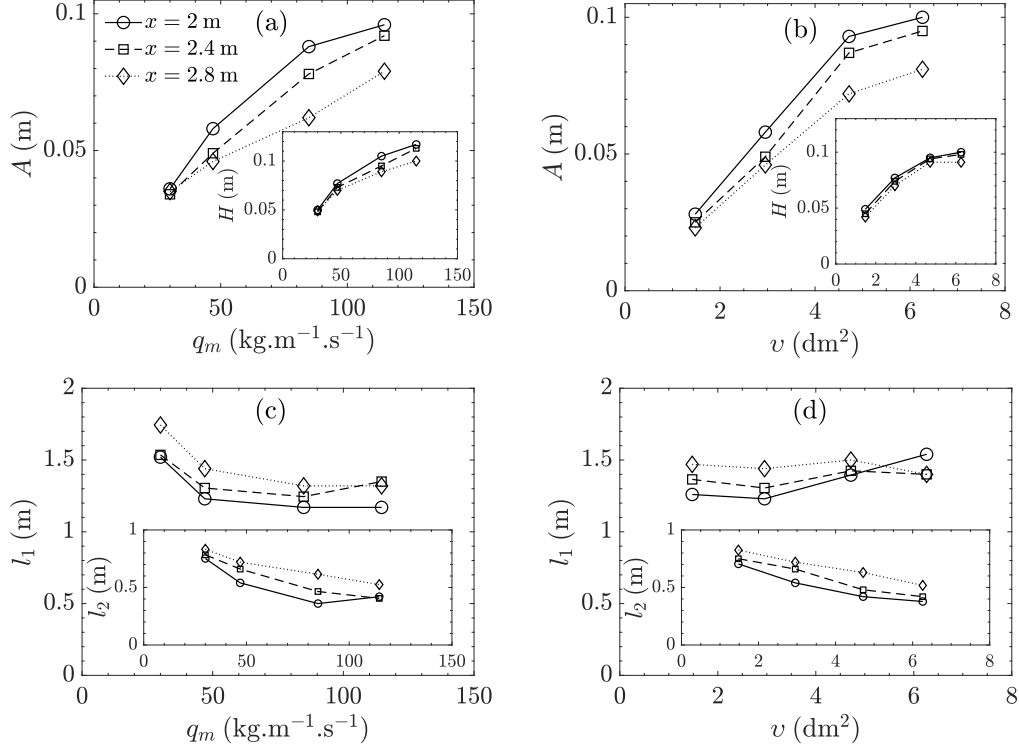


Figure 7. (a,b) Wave amplitude A (inset: wave height H) and (c,d) crest length l_1 (inset: half-amplitude length l_2) as a function of (a,c) the mass flux per width q_m ($v \sim 3.1 \text{ dm}^2$) and (b,d) the volume per width v ($q_m \sim 46 \text{ kg.m}^{-1}.\text{s}^{-1}$), at $x = 2 \text{ m}$, $x = 2.4 \text{ m}$, and $x = 2.8 \text{ m}$ from the shoreline, with $\theta = 15^\circ$ and $H_o = 26.5 \text{ cm}$.

414 propagation, the strong decrease of A is therefore associated to an increase of the wave
 415 trough, to explain the low decrease of H .

416 While the amplitude A and the height H represent the characteristic dimensions
 417 of the wave in the vertical direction, the crest length l_1 and the half-amplitude length
 418 l_2 correspond to those in the horizontal direction. Overall, the crest length l_1 varies slightly
 419 with q_m and v , in the range of parameters considered (Figures 7c and 7d). Except for
 420 $q_m \sim 30 \text{ kg.m}^{-1}.\text{s}^{-1}$, l_1 is roughly constant and equal to $l_1 \sim 1.2 - 1.4 \text{ m}$. By contrast,
 421 the half-amplitude length l_2 decreases for increasing q_m and v (insets of Figures
 422 7c and 7d). In particular, l_2 decreases roughly by a factor 2 when both q_m and v are in-
 423 creased by a factor 4. It can be concluded that, for increasing q_m and v , the amplitude
 424 A and the half-amplitude length l_2 increases and decreases, respectively, leading to steeper
 425 leading waves. Finally, both lengths l_1 and l_2 increase during the wave propagation from
 426 $x = 2 \text{ m}$ (solid lines with circles) to $x = 2.8 \text{ m}$ (dotted lines with diamonds), in agree-
 427 ment with the decrease of the wave amplitude A , by mass conservation.

428 5.3 Role of the maximum water depth

429 At $x = 2 \text{ m}$ to $x = 2.8 \text{ m}$ from the shoreline, it has been previously shown that
 430 the wave types obtained correspond to Stokes and cnoidal waves in the intermediate wa-
 431 ter depth conditions. It is therefore probable that the maximum water depth H_o affects
 432 the generation and the propagation of the leading and largest wave. Up to $x/l_1 \sim 2$

433
434

from the shoreline, its influence is now investigated while other control parameters are kept constant.

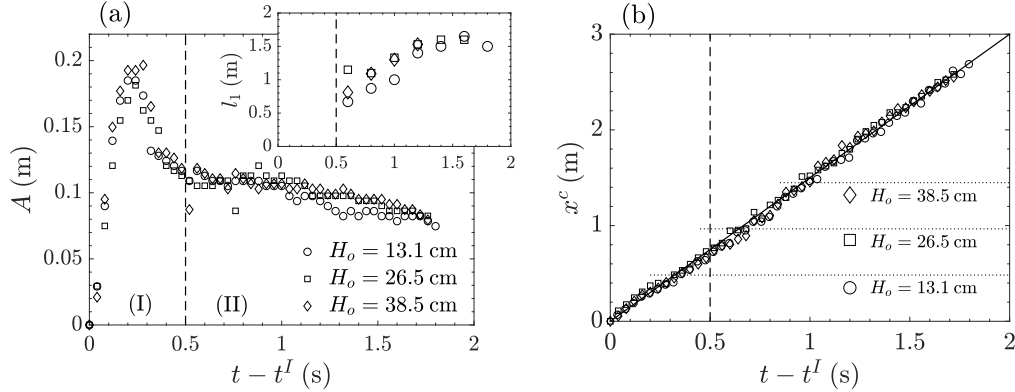


Figure 8. (a) Amplitude A (inset: crest length l_1) and (b) horizontal position of the crest x^c as a function of $t - t^I$, with t^I the time at which the granular flow impacts water, for different maximum water depths H_o . The other parameters are $q_m \sim 47$ kg.m $^{-1}$.s $^{-1}$, $v \sim 6.4$ dm 2 and $\theta = 15^\circ$. (- - -) delimits (I) the generation of the vertical granular jet, and (II) the propagation of the leading and largest wave. In (b), (—) $c = dx^c/dt = 1.5$ m.s $^{-1}$; (···) position of the slope break depending on H_o .

435
436
437
438
439
440
441
442
443
444
445
446
447
448
449

Figure 8(a) shows the temporal evolution of the amplitude A for different maximum water depths H_o . First, the temporal evolution of A is similar for the three different water depths considered. In particular, two distinct phases can be distinguished. Stage (I) corresponds to the generation of the vertical granular jet by the impact of the flow into water. Note that, during this stage, the amplitude A corresponds to the maximum elevation of the granular jet, and it does not represent the wave amplitude. The granular jet elevates until it reaches a height of about 0.2 m and then it falls back on the leading wave. Even if we do not have access to the growth of the leading and largest wave close to the impact, it can be concluded that the maximum wave amplitude is reached in a short time lower than 0.5 s after the impact, in agreement with previous works (Heller et al., 2016; Clous & Abadie, 2019; Bullard, Mulligan, Carreira, & Take, 2019). Stage (II) corresponds to the wave propagation for which the amplitude A and the crest length l_1 (inset of Figure 8a) decreases and increases, respectively. Up to $t - t^I \sim 1.8$ s, with t^I the time at which the granular flow impacts water, the temporal evolution of the length scales of the wave is independent on H_o .

450
451
452
453
454
455
456
457
458
459
460
461
462

Figure 8(b) shows the temporal evolution of the horizontal position of the wave crest, defined as $x^c = x(y = A)$, for different maximum water depths H_o . The dotted lines indicate the location of the slope break, at the transition from the immersed inclined plane to the horizontal bottom, depending on H_o . Once again, the propagation of the wave crest is independent on H_o , and in particular, the crest position evolves linearly with the time meaning a constant crest velocity. More specifically, it is found $c = dx^c/dt = 1.5$ m.s $^{-1}$ (solid line). Unfortunately, no correlation is obtained with different control parameters of the flow and further work will be necessary. For all experiments in the present study, the crest velocity is roughly constant and equal to $c \sim 1.5 \pm 0.3$ m.s $^{-1}$. For comparison, the typical velocity of small-amplitude waves in shallow water gives $\sqrt{gH_o} = [1.1 : 1.9]$ m.s $^{-1}$ in the range of maximum water depths considered here. In the limit of our experimental conditions, this relation gives a fairly good estimate of the crest velocity, despite the crude assumptions.

463 In the near-field region, the independency of the generation and of the propaga-
 464 tion of the leading and largest wave on the maximum water depth H_o can be explained
 465 as follows. The impact of a fluidized granular flow into water generates a wave in a short
 466 time, less than 0.5 s as discussed previously. Moreover, the wave generation mainly oc-
 467 curs on the immersed inclined plane so that the maximum water depth, far away from
 468 the shoreline, can therefore be first disregarded. It is important to recall that the H_o -
 469 independency of wave features is observed in the near-field region, at least up to $x/l_1 \sim$
 470 2 from the shoreline. At sufficiently long times and far enough from the shoreline, it is
 471 expected that the H_o dependency of the wave will be recovered, as already shown in the
 472 case of water flows entering water (Bullard, Mulligan, Carreira, & Take, 2019; Bullard,
 473 Mulligan, & Take, 2019). However, the distance required is probably too large with re-
 474 spect to the dimensions of our experimental setup to observe this near- to far-field tran-
 475 sition, in the range of parameters considered here.

476 6 Comparison with dry granular and water flows

477 In the previous sections, it has been shown that, in the near-field region, the wave
 478 features are mostly controlled by the mass flux q_m and the volume v of the fluidized gran-
 479 ular flow, while the maximum water depth H_o can be disregarded. In this way, the ques-
 480 tions raised are the following. Does the nature of the flowing material affect the wave
 481 features? Are there differences between dry (nonfluidized) granular flows, fluidized gran-
 482 ular flows or water flows in the wave generation?

483 6.1 Flow dynamics at the impact

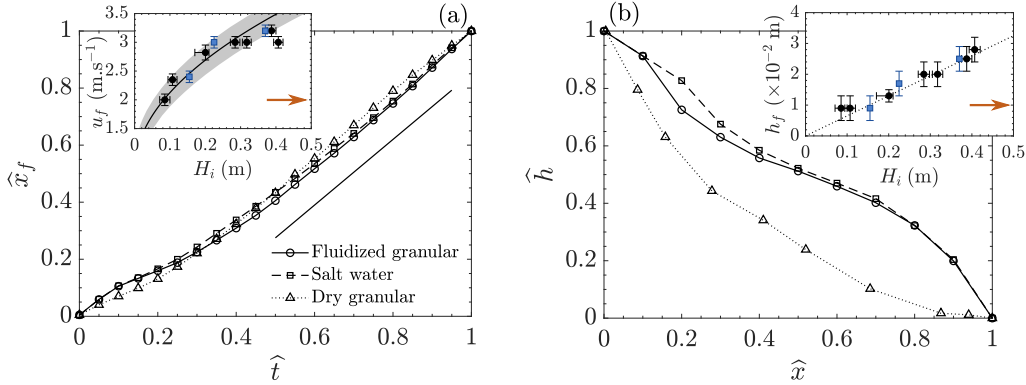


Figure 9. (a) Temporal evolution of the front position \hat{x}_f and (b) typical height profile \hat{h} at the impact, for fluidized granular, dry granular, and salt water flows, in a dimensionless form (equation (3)). In (a), (—) $\hat{x}_f = 1.15\hat{t}$. Insets: (a) constant flow front-velocity u_f and (b) front-height h_f at the impact, as a function of the initial height H_i of the column for fluidized granular (black circles) and salt water (blue squares) flows, with $\theta = 15^\circ$. The orange arrows indicate the value of u_f and h_f , with $H_i \sim 0.8$ m, for a dry granular flow. The solid line, gray area and dotted line are defined in the caption of Figure 3.

Before addressing the wave amplitude as a function of the flowing material, the typical dynamics of dry granular, fluidized granular, and salt water flows is investigated. For the sake of simplicity and only in this section, the origin of the coordinate system (x, y) is shifted at the position of the sluice gate along the inclined plane. In this way, dimen-

sionless variables can be defined as

$$\hat{x} = \frac{x}{x^I}, \quad \hat{h} = \frac{h(x, t^I)}{h(0, t^I)}, \quad \hat{t} = \frac{t}{t^I}, \quad (3)$$

where x^I and t^I correspond to the position of the shoreline and the time at which the granular flow impacts water, respectively.

Figure 9a shows the normalized front position \hat{x}_f as a function of the normalized time \hat{t} , for dry granular, fluidized granular, and salt water flows. In the latter two cases, the curve corresponds to the average of three experiments with different mass flux per width and volume per width in the range $q_m = [26 : 116] \text{ kg.m}^{-1}.\text{s}^{-1}$ and $v = [5.2 : 13.2] \text{ dm}^2$, respectively. The temporal evolution of the front position collapses on a single curve, regardless of the flowing material. In each case, the front accelerates before to reach a constant-front velocity $\hat{x}_f = 1.15\hat{t}$ (solid line), until entering water. Moreover, the trend of the constant flow front-velocity u_f with the initial height of the column H_i is similar for fluidized granular (black circles) and salt water (blue squares) flows, as shown in the inset of Figure 9a. In the case of dry granular flows, however, u_f is much lower compared to fluidized granular and salt water flows, for a given H_i . More specifically, for a dry granular flow, $u_f \sim 2.0 \text{ m.s}^{-1}$ with $H_i \sim 0.8 \text{ m}$ (orange arrow), which is outside the range shown in the inset of Figure 9a.

Figure 9(b) shows the typical height profile \hat{h} of fluidized granular, salt water, and dry granular flows at the impact, for the same set of experiments. First, the height profile of dry granular flows is strongly different from that of fluidized granular and salt water flows. Indeed, the height profile of dry granular flows is concave upward with a height that tends rapidly toward zero, while it is more convex upward with a thick front for fluidized granular and salt water flows. In the latter two cases, the height profile matches very well together, which supports similar dynamics of fluidized granular and water flows, as previously observed in the dam-break configuration on a horizontal plane (Roche et al., 2008). Note that the differences on the height profile morphology between dry granular flows and fluidized granular/salt water flows could affect the dynamics at the impact. Additionally, the trend of the front-height h_f as a function of the initial height H_i of the column is similar for fluidized granular (black circles) and salt water (blue squares) flows, unlike for dry granular flows (orange arrow) (inset in Figure 9b).

6.2 Predictive models for the wave amplitude

Now, the role of the flowing material on the amplitude of the leading and largest wave can be addressed. In particular, the wave amplitude is regarded as a function of dimensionless parameters, namely the Froude number Fr , the relative thickness S , and the relative mass M , according to previous works (Fritz et al., 2004; Zweifel et al., 2006; Heller & Hager, 2010; Zitti et al., 2016; Bullard, Mulligan, Carreira, & Take, 2019). In the following, the wave amplitude A corresponds to the mean value measured at $x = 2, 2.4, \text{ and } 2.8 \text{ m}$ from the shoreline, while error bars indicate the variation. Values of the dimensionless parameters and of the wave amplitudes are provided in the supporting information (Table S1).

Figure 10a shows the normalized wave amplitude A/H_o as a function of the impulse product parameter P , for fluidized granular, dry granular, and salt water flows (see legend in Figure 10c). The dashed-dotted line corresponds to the predictive model $A/H_o = 4P^{4/5}/9$, proposed by Heller and Hager (2010). Note that, for dry granular flows, the volume per width v corresponds to the effective volume entering water, as a granular deposit forms on the subaerial ramp with a slope angle $\theta < \alpha_r$. Qualitatively, both the experimental data and the predictive model follow a similar trend, with in particular, A/H_o increasing for P increasing. Additionally, the scatter of results is included in the inaccuracy range of $\pm 30\%$, observed by Heller and Hager (2010). Quantitatively, however, the general trend of experimental data is underestimated by the predictive model.

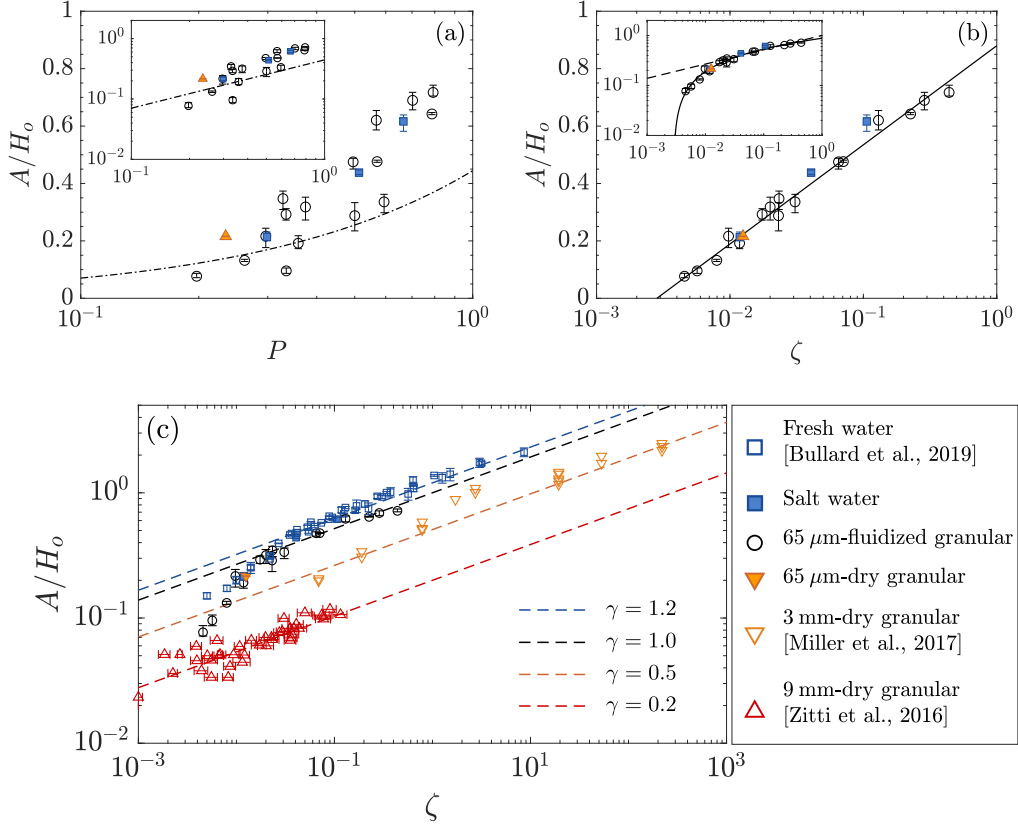


Figure 10. Dimensionless amplitude A/H_o as a function of (a) the impulse product parameter P (equation (1)) and (b,c) the parameter ζ (equation (4)) for different flowing materials (insets: log-log representation). In (a), (---) $A/H_o = 4P^{4/5}/9$ (Heller & Hager, 2010). In (b), (—) $A/H_o = 0.15 \ln \zeta + 0.88$. In (b) and (c), (---) $A/H_o = \gamma \zeta^{2/7}$.

532 Moreover, the dimensionless parameter P leads to a significant inaccuracy on the esti-
 533 mate of the wave amplitude.

To improve the predictive model here, the exponents of equation (1) are set to obtain the best fit with our experimental results, in the case of fluidized granular flows. A better agreement is also obtained considering the vertical component of the flow velocity $u_f \sin \theta$, which differs from previous studies that considered the horizontal component (Zweifel et al., 2006; Heller & Hager, 2010; Mulligan & Take, 2017). This may be discussed considering end-member configurations: A flow at slope angle of $\theta = 0^\circ$ would travel at the water surface without significant basal shear, whereas a flow impacting the water surface at $\theta = 90^\circ$ would cause displacement of the fluid enhancing the wave generation. Thus, we redefine the dimensionless number such as

$$\zeta = \left(\frac{u_f}{\sqrt{gH_o}} \right) \left(\frac{h_f}{H_o} \right) \left(\frac{\rho}{\rho_f} \frac{v}{H_o^2} \right) \sin \theta = FrSM \sin \theta. \quad (4)$$

534 With this redefined parameter, the effect of the mass flux per width $q_m = \rho u_f h_f$ and
 535 of the volume per width v of similar magnitude on the wave amplitude A is recovered,
 536 that is, $\zeta \propto q_m v$.

537 Figure 10b shows the normalized amplitude A/H_o as a function of the dimensionless
 538 parameter ζ , for fluidized granular, dry granular, and salt water flows. First, the pa-

parameter ζ allows to collapse all data for fluidized granular flows on a master curve with a low inaccuracy of $\pm 5\%$. A gross estimate gives $A/H_o = 0.15 \ln \zeta + 0.88$ (solid line). More precisely, for $\zeta \gtrsim 0.02$, the data of fluidized granular flows collapse on a slope $2/7$ (dashed line in inset of Figure 10b), leading to $A/H_o \sim \zeta^{2/7} \sim 1/H_o$. At large ζ , the H_o independency of the leading wave amplitude in the near-field region, as previously mentioned in section 5.3, is therefore recovered. The experimental data deviate from the slope $2/7$, at $\zeta \lesssim 0.02$. Secondly, our data for fluidized granular, dry granular and salt water flows collapse on the master curve. In the range of parameters considered here, our experiments provide the unexpected result that the nature of the flowing material can be disregarded to predict the wave amplitude, and only the flow conditions (e.g., bulk density, volume, and velocity) have to be considered. The phenomenon of wave generation is therefore partly controlled by the flow kinematics, which depends on source conditions and material properties. Our results suggest also that ash-rich pyroclastic flows can be considered as single-phase media in the context of experimental and numerical modeling. However, some caution is required as only the wave amplitude has been considered here.

A further step is to confront our results with data available in the literature, under different flow conditions. Zitti et al. (2016), Miller et al. (2017), and Bullard, Mulligan, Carreira, and Take (2019) investigated the wave generation by 9 mm-positively buoyant granular, 3 mm-negatively buoyant granular, and fresh water flows, respectively. Note that Miller et al. (2017) and Bullard, Mulligan, Carreira, and Take (2019)'s data can be compared directly together, as the experiments were performed in the same conditions (experimental setup, measurement method). In the case of fresh water flows, the data match fairly well with that of our experiments that involved salt water, 65 μm -fluidized granular and 65 μm -dry granular flows. In particular, the case of fresh and salt water flows collapse very well together, while the method to estimate the thickness and the velocity of the flow, in both studies, is slightly different. Overall, at large ζ , it is obtained $A/H_o = \gamma \zeta^{2/7}$, with $\gamma = 1.0$ for the present study, and $\gamma = 1.2$ for that of Bullard, Mulligan, Carreira, and Take (2019). In contrast, the leading and largest waves generated by coarse granular flows are significantly smaller, with $\gamma = 0.5$ and $\gamma = 0.2$ for 3 mm-dry granular (Miller et al., 2017) and 9 mm-dry granular (Zitti et al., 2016) flows, respectively (notice that the data correspond to the maximum values of A/H_o). The influence of the grain size on the wave amplitude may be attributed to the porosity of the flowing material, and more particularly, the ability of water to penetrate it. At sufficiently low grain size, the granular flow is equivalent to a nonporous flowing material, leading to a water-like behavior with an efficient energy transfer between the flow and the water body. In contrast, at larger grain size, the energy of the flow transferred to the leading wave is reduced by water penetrating into the granular medium. In this context, it is important to point out that the ability of a liquid (if it is not water) to penetrate a granular material depends on both grain and liquid properties (e.g., viscosity, size and density of grains, and surface tension).

7 Conclusion

Novel laboratory experiments on the entrance of fluidized granular flows into water have been carried out, for the purpose of better understanding tsunamis generated by pyroclastic flows. The fluidization process aimed at generating high interstitial gas pore pressure, which is thought to be one of the main cause of the high mobility of pyroclastic flows, was considered to ensure a suitable modeling. In the present study, the mass flux per width q_m and the volume per width v of the granular flow, the maximum water depth H_o and the slope angle θ of the inclined plane were varied.

Preliminary observations first showed that the impact of a fluidized granular flow into water led to (i) an initial single vertical granular jet over water, (ii) a leading wave, corresponding to the largest one, which may be followed by low-amplitude waves, and

(iii) a turbulent mixing zone forming a turbidity current. This study focused on the description of the leading and largest wave features and disregarded the flow dynamics of the turbidity current. It was shown that the wave features were mainly controlled by q_m and v with the same order of magnitude. More specifically, at low q_m and v , a smooth, slightly nonlinear, moderate-amplitude leading wave followed by low-amplitude waves was obtained while, at large q_m and v , only a single steep, strongly nonlinear, large-amplitude wave was observed. Overall, the wave types obtained were Stokes to cnoidal in the intermediate water depth conditions, in the range of parameters considered. Additionally, it was shown that the maximum water depth H_o did not affect the wave features in the near-field region. In particular, the wave velocity was independent on H_o , at least up to a distance of $x/l_1 \sim 2$ from the shoreline. Finally, the amplitude of the leading wave generated by fluidized granular, dry granular (nonfluidized) and water flows was compared. To this end, a dimensionless parameter was defined as $\zeta = FrSM \sin \theta$, depending on the Froude number Fr , the relative flow thickness S , the relative mass M , and the slope angle θ . With this parameter, the data for fluidized granular flows collapsed on a master curve with a low inaccuracy of $\pm 5\%$. For $\zeta \gtrsim 0.02$, the dimensionless amplitude A/H_o scaled as $1/H_o$, hence supporting the H_o -independency in the near-field region. Moreover, this scaling law was used to compare the waves generated by dry granular, fluidized granular, or water flows entering water. It was first shown that the flow dynamics of fine-grained fluidized granular and water flows were strictly equivalent at the impact, differing clearly from dry granular flows. Secondly, fine-grained fluidized, fine-grained dry and water flows generated similar leading wave amplitudes. In contrast, coarse granular flows generate lower wave amplitudes, which was attributed to the ability of water to penetrate the flowing material, depending on both the grain and liquid (if it is not water) properties.

In the geophysical context, the present study showed that the wave features may be mainly controlled by both the flow dynamics and the volume of gravity-driven flows that enter water. It is therefore expected that rapid flows, like pyroclastic density currents and debris flows, generate larger waves than other natural flows, for a similar volume. Moreover, the ability of water to penetrate such flows could affect the wave amplitude. For the purpose of volcanic tsunamis, pyroclastic flows are usually composed of a large amount of fine ash and may have high gas pore pressure, two factors likely to prevent the penetration of water into the flow. Such flows are therefore expected to promote the generation of large tsunamis. Finally, this study provided the unexpected result that ash-rich pyroclastic flows can be considered as single-phase media in the context of experimental and numerical studies.

Acknowledgments

This work was funded by the ANR RAVEX (ANR-16-CE03-0002) project. This is Cler-Volc contribution no. 405. The authors acknowledge the support of the technical staff of the Laboratoire Magmas et Volcans (M. Nivoix, E. Brut, J.-L. Fruquière, C. Guillot) for their contribution in designing and constructing the experimental setup. A. Bougouin is grateful to S. Abadie, M. Cabrera, H. E. Huppert, L. Lacaze, Y. Le Guer, and S. Virolet for fruitful discussions. We thank R. P. Mulligan and F. Løvholt for the constructive comments that helped to greatly improve the initial manuscript. Data presented in this paper are in open access at

<https://doi.org/10.6084/m9.figshare.10070183.v1>.

References

- Allen, S. R., Freundt, A., & Kurokawa, K. (2012). Characteristics of submarine pumice-rich density current deposits sourced from turbulent mixing of sub-aerial pyroclastic flows at the shoreline: field and experimental assessment. *Bull. Volcanol.*, *74*, 657–675.

- 642 Ancey, C., Iverson, R. M., Rentschler, M., & Denlinger, R. P. (2008). An exact
643 solution for ideal dam-break floods on steep slopes. *Water Resour. Res.*, *44*,
644 W01430.
- 645 Ataie-Ashtiani, B., & Nik-Khah, A. (2008). Impulsive waves caused by subaerial
646 landslides. *Env. Fluid Mech.*, *8*, 263–280.
- 647 Bonometti, T., Balachandar, S., & Magnaudet, J. (2008). Wall effects in non-
648 Boussinesq density currents. *J. Fluid Mech.*, *616*, 445–475.
- 649 Bougouin, A., Lacaze, L., & Bonometti, T. (2017). Collapse of a neutrally buoyant
650 suspension column: from Newtonian to apparent non-Newtonian flow regimes.
651 *J. Fluid Mech.*, *826*, 918–941.
- 652 Bougouin, A., Paris, R., & Roche, O. (2019). Ecoulement granulaire fluidisé impac-
653 tant l’eau: Application aux tsunamis volcaniques. In *24ème congrès français de*
654 *mécanique*.
- 655 Breard, E. C. P., Dufek, J., & Lube, G. (2018). Enhanced mobility in concentrated
656 pyroclastic density currents: An examination of a self-fluidization mechanism.
657 *Geophys. Res. Lett.*, *45*, 654–664.
- 658 Bullard, G. K., Mulligan, R. P., Carreira, A., & Take, W. A. (2019). Experimental
659 analysis of tsunamis generated by the impact of landslides with high mobility.
660 *Coast. Eng.*, *152*, 103538.
- 661 Bullard, G. K., Mulligan, R. P., & Take, W. A. (2019). An enhanced framework to
662 quantify the shape of impulse waves using asymmetry. *J. Geophys. Res.*, *124*,
663 652–666.
- 664 Carey, S., Morelli, D., Sigurdsson, H., & Bronto, S. (2001). Tsunami deposits from
665 major explosive eruptions: An example from the 1883 eruption of Krakatau.
666 *Geology*, *29*, 347–350.
- 667 Chédeville, C., & Roche, O. (2014). Autofluidization of pyroclastic flows propagat-
668 ing on rough substrates as shown by laboratory experiments. *J. Geophys. Res.*,
669 *119*, 1764–1776.
- 670 Chédeville, C., & Roche, O. (2018). Autofluidization of collapsing bed of fine par-
671 ticles: Implications for the emplacement of pyroclastic flows. *J. Volcanol.*
672 *Geotherm. Res.*, *368*, 91–99.
- 673 Clous, L., & Abadie, S. (2019). Simulation of energy transfers in waves generated by
674 granular slides. *Landslides*, *16*, 1663–1679.
- 675 De Lange, W. P., Prasetya, G. S., & Healy, T. R. (2001). Modelling of tsunamis gen-
676 erated by pyroclastic flows (ignimbrites). *Nat. Hazards*, *24*, 251–266.
- 677 Delannay, R., Valance, A., Mangeney, A., Roche, O., & Richard, P. (2017). Granular
678 and particle-laden flows: from laboratory experiments to field observations. *J.*
679 *Phys. D*, *50*, 053001.
- 680 Dressler, R. F. (1952). Hydraulic resistance effect upon the dam-break functions. *J.*
681 *Res. Natl. Bur. Stand.*, *49*, 217–225.
- 682 Dressler, R. F. (1954). Comparison of theories and experiments for the hydraulic
683 dam-break wave. *Int. Assoc. Sci. Hydrology*, *3*, 319–328.
- 684 Dufek, J. (2016). The fluid mechanics of pyroclastic density currents. *Ann. Rev.*
685 *Fluid Mech.*, *48*, 459–485.
- 686 Dufek, J., & Manga, M. (2008). In situ production of ash in pyroclastic flows. *J.*
687 *Geophys. Res.*, *113*, B09207.
- 688 Farin, M., Mangeney, A., & Roche, O. (2014). Fundamental changes of granular flow
689 dynamics, deposition, and erosion processes at high slope angles: Insights from
690 laboratory. *J. Geophys. Res.*, *119*, 504–532.
- 691 Freundt, A. (2003). Entrance of hot pyroclastic flows into the sea: Experimental ob-
692 servations. *Bull. Volcanol.*, *65*, 144–164.
- 693 Fritz, H. M., Hager, W. H., & Minor, H.-E. (2003a). Landslide generated impulse
694 waves. 1. Instantaneous flow fields. *Exp. Fluids*, *35*, 505–519.
- 695 Fritz, H. M., Hager, W. H., & Minor, H.-E. (2003b). Landslide generated impulse
696 waves. 2. Hydrodynamic impact craters. *Exp. Fluids*, *35*, 520–532.

- 697 Fritz, H. M., Hager, W. H., & Minor, H.-E. (2004). Near field characteristics of
698 landslide generated impulse waves. *J. Waterway, Port, Coast. Ocean Eng.*,
699 *130*, 287–302.
- 700 Girolami, L., Druitt, T. H., Roche, O., & Khrabrykh, Z. (2008). Propagation and
701 hindered settling of laboratory ash flows. *J. Geophys. Res.*, *113*, B02202.
- 702 Gouhier, M., & Paris, R. (2019). SO₂ and tephra emissions during the December 22,
703 2018 Anak Krakatau flank-collapse eruption. *Volcanica*, *2*, 91–103.
- 704 Gravish, N., & Goldman, D. I. (2014). Effect of volume fraction on granular
705 avalanche dynamics. *Phys. Rev. E*, *90*, 032202.
- 706 Grezio, A., Babeyko, A., Baptista, M. A., Behrens, J., Costa, A., Davies, G., ...
707 Kie Thio, H. (2017). Probabilistic tsunami hazard analysis: Multiple sources
708 and global applications. *Rev. Geophys.*, *55*, 1158–1198.
- 709 Grilli, S. T., Tappin, D. R., Carey, S., Watt, S. F. L., Ward, S. N., Grilli, A. R., ...
710 Muin, M. (2019). Modelling of the tsunami from the December 22, 2018 lat-
711 eral collapse of Anak Krakatau volcano in the Sunda Straits, Indonesia. *Sci.*
712 *Reports*, *9*, 11946.
- 713 Harbitz, C. B., Løvholt, F., Pedersen, G., & Masson, D. G. (2006). Mechanisms
714 of tsunami generation by submarine landslides: a short review. *Nor. J. Geol.*,
715 *86*(3).
- 716 Heinrich, P. (1992). Nonlinear water waves generated by submarine and aerial land-
717 slides. *J. Waterway, Port, Coast. Ocean Eng.*, *118*, 249–266.
- 718 Heller, V., Bruggemann, M., Spinneken, J., & Rogers, B. D. (2016). Composite
719 modelling of subaerial landslide-tsunamis in different water body geometries
720 and novel insight into slide and wave kinematics. *Coast. Eng.*, *109*, 20–41.
- 721 Heller, V., Chen, F., Brühl, M., Gabl, R., Chen, X., Wolters, G., & Fuchs, H.
722 (2019). Large-scale experiments into the tsunamigenic potential of different
723 iceberg calving mechanisms. *Sci. Rep.*, *9*.
- 724 Heller, V., & Hager, W. H. (2010). Impulse product parameter in landslide gener-
725 ated impulse waves. *J. Waterway, Port, Coast. Ocean Eng.*, *136*, 145–155.
- 726 Heller, V., & Hager, W. H. (2011). Wave types of landslide generated impulse waves.
727 *Ocean Eng.*, *38*, 630–640.
- 728 Heller, V., & Kinnear, R. D. (2010). Discussion of Experimental investigation of im-
729 pact generated tsunami; related to a potential rock slide, Western Norway by
730 G. Sælevik, A. Jensen, G. Pedersen [Coastal Eng. 56 (2009) 897–906]. *Coast.*
731 *Eng.*, *57*, 773–777.
- 732 Heller, V., & Spinneken, J. (2015). On the effect of the water body geometry on
733 landslide–tsunamis: Physical insight from laboratory tests and 2D to 3D wave
734 parameter transformation. *Coast. Eng. J.*, *104*, 113–134.
- 735 Hogg, A. J., & Pritchard, D. (2004). The effects of hydraulic resistance on dam-
736 break and other shallow inertial flows. *J. Fluid Mech.*, *501*, 179–212.
- 737 Hogg, A. J., & Woods, A. W. (2001). The transition from inertia- to bottom-
738 drag-dominated motion of turbulent gravity currents. *J. Fluid Mech.*, *449*,
739 201–224.
- 740 Jánosi, I. M., Jan, D., Szabó, K. G., & Tél, T. (2004). Turbulent drag reduction in
741 dam-break flows. *Exp. Fluids*, *37*, 219–229.
- 742 Kamphuis, J. W., & Bowering, R. J. (1970). Impulse waves generated by landslides.
743 In *Proc. of 12th Coastal Engineering Conference, New York, United States*.
- 744 Kneller, B., & Buckee, C. (2000). The structure and fluid mechanics of turbidity
745 currents: a review of some recent studies and their geological implications.
746 *Sedimentology*, *47*, 62–94.
- 747 Latter, J. H. (1981). Tsunamis of volcanic origin: Summary of causes, with particu-
748 lar reference to Krakatoa, 1883. *Bull. Volcanol.*, *44*, 467–490.
- 749 Law, L., & Brebner, A. (1968). On water waves generated by landslides. In *Proc.*
750 *of the Third Australasian Conference on Hydraulics and Fluid Mechanics,*
751 *Sydney, Australia*.

- 752 Lay, T., Kanamori, H., Ammon, J., Nettles, M., Ward, S. N., Aster, R. C., . . . Sip-
753 kin, S. (2005). The great Sumatra-Andaman earthquake of 26 december 2004.
754 *Science*, *308*, 1127–1133.
- 755 Leal, J. G., Ferreira, R. M., & Cardoso, A. H. (2006). Dam-break wave-front veloc-
756 ity. *J. Hydraul. Res.*, *132*, 69–76.
- 757 Le Méhauté, B. (1976). *An introduction to hydrodynamics and water waves*.
758 Springer, New York.
- 759 Lindstrøm, E. K. (2016). Waves generated by subaerial slides with various porosi-
760 ties. *Coast. Eng. J.*, *116*, 170–179.
- 761 Løvholt, F., Pedersen, G., Harbitz, C. B., Glimsdal, S., & Kim, J. (2015). On the
762 characteristics of landslide tsunamis. *Phil. Trans. R. Soc. A*, *373*, 20140376.
- 763 Lube, G., Breard, E. C. P., Jones, J., Fullard, L., Dufek, J., Cronin, S. J., & Wang,
764 T. (2019). Generation of air lubrication within pyroclastic density currents.
765 *Nat. Geosci.*, *12*, 381–386.
- 766 Maeno, F., & Imanura, F. (2011). Tsunami generation by a rapid entrance of pyro-
767 clastic flow into the sea during the 1883 Krakatau eruption, Indonesia. *J. Geo-
768ophys. Res.*, *116*, B09205.
- 769 Mangeney, A., Roche, O., Hungr, O., Mangold, N., Faccanoni, G., & Lucas, A.
770 (2010). Erosion and mobility in granular collapse over sloping beds. *J. Geo-
771ophys. Res.*, *115*, F03040.
- 772 Mattioli, G. S., Voight, B., Linde, A. T., Sacks, I. S., Watts, P., Widiwijayanti, C.,
773 . . . Williams, D. (2007). Unique and remarkable dilatometer measurements of
774 pyroclastic flow-generated tsunamis. *Geology*, *35*, 25–28.
- 775 McCowan, J. (1894). On the highest wave of permanent type. *Philos. Mag. Series 5*,
776 *38*, 351–358.
- 777 Michell, J. H. (1893). The highest waves in water. *Philos. Mag. Series 5*, *36*, 430–
778 437.
- 779 Miller, G. S., Andy T., W., Mulligan, R. P., & McDougall, S. (2017). Tsunamis gen-
780 erated by long and thin granular landslides in a large flume. *J. Geophys. Res.*,
781 *122*, 653–668.
- 782 Mohammed, F., & Fritz, H. M. (2012). Physical modeling of tsunamis generated
783 by three-dimensional deformable granular landslides. *J. Geophys. Res.*, *117*,
784 C11015.
- 785 Monaghan, J. J., Kos, A., & Issa, N. (2003). Fluid motion generated by impact. *J.*
786 *Waterway, Port, Coast. Ocean Eng.*, *129*.
- 787 Montserrat, S., Tamburrino, A., Roche, O., & Niño, Y. (2012). Pore fluid pressure
788 diffusion in defluidizing granular columns. *J. Geophys. Res.*, *117*, F02034.
- 789 Mulligan, R. P., & Take, W. A. (2017). On the transfer of momentum from a granu-
790 lar landslide to a water wave. *Coast. Eng.*, *125*, 16–22.
- 791 Nishimura, Y., Nakagawa, M., Kuduon, J., & Wukawa, J. (2005). Timing and scale
792 of tsunamis caused by the 1994 Rabaul eruption, East New Britain, Papua
793 New Guinea. In *Tsunamis* (pp. 43–56). Springer.
- 794 Nomanbhoy, N., & Satake, K. (1995). Generation mechanism of tsunamis from the
795 1883 Krakatau eruption. *Geophys. Res. Lett.*, *22*, 509–512.
- 796 Nomikou, P., Druitt, T. H., Hübscher, C., Mather, T. A., Paulatto, M., Kalnins,
797 L. M., . . . Parks, M. M. (2016). Post-eruptive flooding of Santorini caldera
798 and implications for tsunami generation. *Nat. Commun.*, *7*, 13332.
- 799 Paris, R. (2015). Source mechanisms of volcanic tsunamis. *Phil. Trans. R. Soc. A*,
800 *373*, 20140380.
- 801 Paris, R., Switzer, A. D., Belousova, M., Belousov, A., Ontowirjo, B., Whelley, P. L.,
802 & Ulvrova, M. (2014). Volcanic tsunami: a review of source mechanisms,
803 past events and hazards in Southeast Asia (Indonesia, Philippines, Papua New
804 Guinea). *Nat. Hazards*, *70*, 447–470.
- 805 Paris, R., Wassmer, P., Lavigne, F., Belousov, A., Belousova, M., Iskandarsyah, Y.,
806 . . . Mazzoni, N. (2014). Coupling eruption and tsunami records: the Krakatau

- 1883 case study, Indonesia. *Bull. Volcanol.*, *76*, 814.
- 807
808 Pelinovsky, E., Zahibo, N., Dunkley, P., Edmonds, M., Herd, R., Talipova, T., . . .
809 Nikolkina, I. (2004). Tsunami generated by the volcano eruption on July
810 12–13, 2003 at Montserrat, Lesser Antilles. *Sci. Tsunami Hazards*, *22*, 44–57.
- 811 Poulighen, O. (1999). Scaling laws in granular flows down rough inclined planes.
812 *Phys. Fluids*, *11*, 542–548.
- 813 Ritter, A. (1892). Die fortpflanzung der wasserwellen. *Z. Verein Deutch. Ing.*, *36*,
814 947–954.
- 815 Roche, O. (2012). Depositional processes and gas pore pressure in pyroclastic flows:
816 an experimental perspective. *Bull. Volcanol.*, *74*, 1807–1820.
- 817 Roche, O., Attali, M., Mangeney, A., & Lucas, A. (2011). On the run-out distance
818 of geophysical gravitational flows: Insight from fluidized granular collapse
819 experiments. *Earth Planet. Sci. Lett.*, *311*, 375–385.
- 820 Roche, O., Gilbertson, M., Phillips, J. C., & Sparks, R. S. J. (2002). Experiments on
821 deaerating granular flows and implications for pyroclastic flow mobility. *Geo-*
822 *phys. Res. Lett.*, *29*, 1792.
- 823 Roche, O., Montserrat, S., Niño, Y., & Tamburrino, A. (2008). Experimental
824 observations of water-like behavior of initially fluidized, dam break granular
825 flows and their relevance for the propagation of ash-rich pyroclastic flows. *J.*
826 *Geophys. Res.*, *113*, B12203.
- 827 Rowley, P. J., Roche, O., Druitt, T. H., & Cas, R. A. F. (2014). Experimental study
828 of dense pyroclastic density currents using sustained, gas-fluidized granular
829 flows. *Bull. Volcanol.*, *76*, 855.
- 830 Smith, G. M., Williams, R., Rowley, P. J., & Parsons, D. R. (2018). Investigation
831 of variable aeration of monodisperse mixtures: Implications for pyroclastic
832 density currents. *Bull. Volcanol.*, *80*, 67.
- 833 Soria-Hoyo, C., Valverde, J. M., & Roche, O. (2019). A laboratory-scale study on
834 the role of mechanical vibrations in pore pressure generation in pyroclastic
835 materials: Implications for pyroclastic flows. *Bull. Volcanol.*, *81*, 12.
- 836 Sparks, R. S. J. (1976). Grain size variations in ignimbrites and implications for the
837 transport of pyroclastic flows. *Sedimentology*, *23*, 147–188.
- 838 Tanguy, J.-C., Ribi re, C., Scarth, A., & Tjetjep, W. S. (1998). Victims from vol-
839 canic eruptions: a revised database. *Bull. Volcanol.*, *60*, 137–144.
- 840 Valverde, J. M., & Soria-Hoyo, C. (2015). Vibration-induced dynamical weakening of
841 pyroclastic flows: Insights from rotating drum experiments. *J. Geophys. Res.*,
842 *120*, 6182–6190.
- 843 Verbeek, R. D. M. (1886). Krakatau. *Imprimerie de l'Etat, Batavia (Indonesia)*.
- 844 Viroulet, S., C bron, D., Kimmoun, O., & Kharif, C. (2013). Shallow water waves
845 generated by subaerial solid landslides. *Geophys. J. Int.*, *193*, 747–762.
- 846 Viroulet, S., Sauret, A., & Kimmoun, O. (2014). Tsunami generated by a granular
847 collapse down a rough inclined plane. *EPL*, *105*, 34004.
- 848 Walder, J. S., Watts, P., Sorensen, O. E., & Janssen, K. (2003). Tsunamis generated
849 by subaerial mass flows. *J. Geophys. Res.*, *108*.
- 850 Watts, P., & Waythomas, C. F. (2003). Theoretical analysis of tsunami generation
851 by pyroclastic flows. *J. Geophys. Res.*, *108*, B12, 2563.
- 852 Wilson, C. J. N. (1980). The role of fluidization in the emplacement of pyroclastic
853 claws: An experimental approach. *J. Volcanol. Geotherm. Res.*, *8*, 231–249.
- 854 W nnemann, K., & Weiss, R. (2015). The meteorite impact-induced tsunami haz-
855 ard. *Phil. Trans. R. Soc. A*, *373*, 20140381.
- 856 Yavari-Ramshe, S., & Ataie-Ashtiani, B. (2016). Numerical modeling of subaerial
857 and submarine landslide-generated tsunami waves-recent advances and future
858 challenges. *Landslides*, *13*, 1325–1368.
- 859 Yokoyama, I. (1987). A scenario of the 1883 krakatau tsunami. *J. Volcanol.*
860 *Geotherm. Res.*, *34*, 123–132.

- 861 Zitti, G., Ancey, C., Postacchini, M., & Brocchini, M. (2016). Impulse waves gen-
862 erated by snow avalanches: Momentum and energy transfer to a water body. *J.*
863 *Geophys. Res.*, *121*, 2399–2423.
- 864 Zweifel, A., Hager, H., & Minor, H.-E. (2006). Plane impulse waves in reservoirs. *J.*
865 *Waterway, Port, Coast. Ocean Eng.*, *132*, 356–368.